



Analysis of Dynamic Fracture Compliance Based on Poroelastic Theory. Part II: Results of Numerical and Experimental Tests

DING WANG,¹ PIN-BO DING,² and JING BA³

Abstract—In Part I, a dynamic fracture compliance model (DFCM) was derived based on the poroelastic theory. The normal compliance of fractures is frequency-dependent and closely associated with the connectivity of porous media. In this paper, we first compare the DFCM with previous fractured media theories in the literature in a full frequency range. Furthermore, experimental tests are performed on synthetic rock specimens, and the DFCM is compared with the experimental data in the ultrasonic frequency band. Synthetic rock specimens saturated with water have more realistic mineral compositions and pore structures relative to previous works in comparison with natural reservoir rocks. The fracture/pore geometrical and physical parameters can be controlled to replicate approximately those of natural rocks. P- and S-wave anisotropy characteristics with different fracture and pore properties are calculated and numerical results are compared with experimental data. Although the measurement frequency is relatively high, the results of DFCM are appropriate for explaining the experimental data. The characteristic frequency of fluid pressure equilibration calculated based on the specimen parameters is not substantially less than the measurement frequency. In the dynamic fracture model, the wave-induced fluid flow behavior is an important factor for the fracture–wave interaction process, which differs from the models at the high-frequency limits, for instance, Hudson’s un-relaxed model.

Key words: Fracture compliance, poroelastic theory, synthetic fractured rock, ultrasonic measurement, wave-induced fluid flow.

1. Introduction

In recent years, elastic wave propagation in fractured porous media has attracted extensive attention in the rock physics community (Müller et al. 2010;

Carcione et al. 2012; Ding et al. 2014; Sarout et al. 2017). Porous rocks containing fractures and viscous fluids cannot be treated as purely elastic materials. Propagating elastic waves dissipate energy in such media. Anelasticity in porous rocks provides an approach for investigating structures and fluid properties in hydrocarbon-saturated reservoirs (Chapman 2003; Wang et al. 2016; Ba et al. 2016, 2017). By incorporating the so-called global fluid flow at the wavelength scale (Biot 1956) and the squirt flow at the pore/grain scale (Hudson et al. 1996; Jakobsen and Chapman 2009; Pride and Berryman 2003; Wang et al. 2016), the wave-induced fluid flow (WIFF) in a porous medium, which is related to the fluid pressure gradient relaxation/un-relaxation at different scales, has been found to be the most important mechanism causing intrinsic wave attenuation and dispersion. The WIFF process of squirt flow in a fractured porous medium is frequency-dependent and is related to the local heterogeneity scale (e.g., the radius or the spacing of fractures) and to the connectivity between fractures and host rock. The pore system of a real fractured rock is generally assumed to consist of stiff pores and soft pores (fractures/cracks). For these rocks, the WIFF between fractures and those intergranular pores is the dominant energy dissipation mechanism, if the wave scattering effects can be neglected at those specific investigation frequencies or scales.

Most of the WIFF theoretical models in the literature are presented to establish the relationship between fracture (or/and structure) parameters and wave response (Hudson et al. 1996; Thomsen 1995; Chapman 2003; Liu et al. 2000; Brajanovski et al. 2005; Guéguen and Sarout 2009, 2011; Guéguen and Kachanov 2011). These theories can be classified into

¹ Center of Rock Mechanics and Geohazards, Shaoxing University, Shaoxing 312000, China.

² State Key Laboratory of Petroleum Resource and Prospecting, China University of Petroleum, Beijing 102249, China.

³ School of Earth Sciences and Engineering, Hohai University, Nanjing 211100, China. E-mail: jba@hhu.edu.cn

two categories: the effective stiffness approach and the compliance superposition approach. The main differences between the two approaches and their advantages were discussed in the previous paper (Wang et al. 2017). Studies have focused on the compliance approach in recent decades. Note that the existing compliance models mainly focus on the dry and sealed (i.e., closed fractures without fluid exchange between the fractures and the pores) fluid-saturated fractures (Sayers and Kachanov 1995; Schoenberg 1980; Schoenberg and Sayers 1995; Verdon et al. 2008). In Part I (Wang et al. 2017), a new fracture compliance model was presented based on the poroelastic theory. The fracture compliance tensor is complex-valued and frequency-dependent due to WIFF between fractures and pores. Using this definition of compliance, we can effectively discriminate different saturating fluids in the fractures even if they have a similar bulk modulus (e.g., water and oil). The effects of solid phase of the host rock on the frequency-dependence characteristics of the normal compliance were then analyzed (Wang et al. 2017). In this paper, the dynamic fracture compliance model (DFCM) is analyzed and validated, and in the comparative analysis, we include the results of the theoretical models published in the literature and the experimental data on the synthetic rock specimens obtained in this study.

One of the fracture models was developed by Brajanovski et al. (2005) using the propagation matrix theory, where they presented the frequency-dependent effective P-wave elastic moduli of a porous rock containing parallel fractures. This model was built based on a simplified physical system consisting of a periodic assemblage of two layers with different poroelastic properties as first proposed by White et al. (1975). It was shown that the fluid exchange between fractures and pores had a significant impact on velocity dispersion and attenuation. In addition, the pressure equilibration time strongly depends on the connectivity of the porous medium and the distance between two neighbouring fractures. In this study, the differences between DFCM and Brajanovski's model are investigated in numerical examples with variable rock parameters.

On the other hand, DFCM is analyzed and validated by comparing with the experimental data from synthetic rocks. The fracture geometry and pore physical parameters can hardly be obtained for natural fractured rocks without destroying the specimens. This is also an issue if natural rocks are used in laboratory experiments to validate the models. The approach of synthetic fractured physical models (the solid materials are mostly organic glass, epoxy resin, and silicone rubber, etc.) was introduced to control fracture properties (de Figueiredo et al. 2013; Rathore et al. 1995). However, the large ratio of fracture dimension to wavelength and the low connectivity of the host rock in these studies were obviously inconsistent with natural rocks (Ass'ad et al. 1992; de Figueiredo et al. 2013). Rathore et al. (1995) made a synthetic sandstone containing fractures of known dimensions and geometry using sand cemented with epoxy glue. The measurement results were compared with the existing theoretical models. However, epoxy glue can cause excessive attenuation and dispersion due to its viscoelastic properties, which differs from the grain cement in natural rocks. This can possibly lead to equivocal interpretation of wave dispersion and attenuation in fractured media. Tillotson et al. (2012) made synthetic silica cemented samples with controlled fracture geometry. Ding et al. (2014) extended Rathore's method and investigated how wave velocities were influenced by fracture density and fluids. Their method can be used to produce samples with mineral composition and cementation, which approach natural rocks.

In this paper, we present two synthetic samples saturated with water and with different fracture densities using Ding's manufacturing method (Ding et al. 2014). One P-wave and two S-wave velocities are measured using the pulse transmission technique. The measurements are compared to the theoretical predictions of the DFCM and of Hudson's high-frequency model. The DFCM also shows a good agreement with Thomsen's low-frequency model (Thomsen 1995), where fluid is allowed to flow between fractures and intergranular pores.

2. Numerical Comparison Results

In this section, the results of a typical compliance model are compared with those of the DFCM. The theoretical models for the WIFF process in fractured porous media in the literature are derived from different physical approximations (Chapman 2003; Liu et al. 2000; Brajanovski et al. 2005; Guéguen and Sarout 2009, 2011; Guéguen and Kachanov 2011). In the DFCM and Brajanovski's model, the fractures are modelled as thin porous layers with different pore structure and petrophysical parameters relative to the host rock. Therefore, the fractures and host rock have a different reaction to an incident wave. A local pressure gradient between fractures and background pores takes place at the interface of fractures. Brajanovski's model is built based on the propagation matrix theory in which the stress (including the fluid pressure) and strain induced by a wave are continuous on the planes of fractures. On the other hand, the DFCM is derived by combining the linear slip method and the poroelasticity theory. In the DFCM, the displacement is discontinuous across a fracture and the fluid flow process is controlled by pressure diffusion equations in a relatively low-frequency region. We compare the numerical results of DFCM with Brajanovski's model for different fracture and matrix parameters in this study.

According to Wang et al. (2017), the explicit expression of the dynamic normal compliance of a fracture was expressed as follows:

$$Z_n = \frac{\zeta_c^{\text{uni}} h_c}{M_c \alpha_c} \left\{ 1 + \frac{G}{\psi \zeta_c^{\text{uni}}} \left[\frac{2}{h_c \sqrt{\frac{i\omega}{D_c}}} \left(e^{\sqrt{\frac{i\omega}{D_c}} h_c} - 1 \right) + \frac{4\kappa_c M_c}{i\omega \eta h_c} \left(e^{\sqrt{\frac{i\omega}{D_c}} h_c} - 1 \right)^2 \right] \right\}. \quad (1)$$

First of all, note that the subscript c in Eq. (1) denotes the physical parameters within the fractures. $\zeta_c^{\text{uni}} = \alpha_c M_c / C_c$, where $M_c = [(\alpha_c - \phi_c) / K^s + \phi_c / K^f]^{-1}$ is the pore space modulus, $\alpha_c = 1 - K_c^{\text{dry}} / K^s$ is the Biot-Willis effective stress coefficient (Biot and Willis 1957), C_c is the compressional P-wave modulus of the fluid-saturated porous medium given by Gassmann's equations. K_c^{dry} , K^s and K^f are the bulk moduli of the skeleton frame,

rock grain, and pore fluid, respectively. h_c is the fracture thickness. The diffusion parameter is given by $D_c = \kappa_c M_c L_c / \eta C_c$, where η is the viscosity coefficient of the pore fluid, κ_c is the permeability of the fractures, and L_c is the dry compressional P-wave modulus. The fluid coupling parameter G is given by the following:

$$G = \frac{1}{\left(1 + e^{\sqrt{\frac{i\omega}{D_m}} h_m} \right) \left[\frac{\kappa_c \sqrt{\frac{i\omega}{D_c}} \left(e^{\sqrt{\frac{i\omega}{D_c}} h_c} - 1 \right)}{\kappa_m \sqrt{\frac{i\omega}{D_m}} \left(1 - e^{\sqrt{\frac{i\omega}{D_m}} h_m} \right)} \right]} - \left(1 + e^{\sqrt{\frac{i\omega}{D_c}} h_c} \right)}, \quad (2)$$

and ψ can be expressed as follows:

$$\psi = \frac{r_c K_c^{\text{sat}} C_m + r_m K_m^{\text{sat}} C_c}{\alpha_m M_m C_c - \alpha_c M_c C_m} (\zeta_c^{\text{uni}} - \zeta_m^{\text{uni}})^{-1}. \quad (3)$$

Similarly, subscript m in Eqs. (2) and (3) denotes the physical parameters within the host rock. The spacing between two neighbouring fractures is H ; $r_c = h_c / H$ and $r_m = h_m / H$ are the fracture and background layer thickness fraction, respectively. The poroelastic parameter $K^{\text{sat}} = K^{\text{dry}} + \alpha^2 M$ is given by Gassmann's equations (Gassmann 1951). Equation (1) shows that in a porous host rock, the variation of compliance of a fracture saturated with a fluid in comparison with the compliance of the dry case is caused by fluid exchange between the fractures and the rock matrix.

We first give and compare the equations of the DFCM and Brajanovski's model in the relaxed and un-relaxed regimes. At both the high- and low-frequency limits, the moduli of fractured media are frequency-independent. Combining Eqs. (1)–(3), the normal compliance of the fractures derived from the DFCM is given as follows:

$$Z_n^{\text{high}} = h_c / C_c, \quad (4)$$

for the high-frequency limit. On the other hand, the effective P-wave modulus perpendicular to the fractures is given by the following:

$$\frac{1}{C_{\text{eff}}} = \frac{1}{C_b} + \frac{Z_n}{H}. \quad (5)$$

Obviously, Z_n^{high} / H is equivalent to the second part (i.e., the fracture compliance) of Eq. (36) in

Brajanovski et al. (2005), as expected. When the angular frequency $\omega \rightarrow 0$, the normal compliance is

$$Z_n^{\text{low}} = \frac{h_c}{C_c} + \frac{h_c G^{\text{low}}}{M_c \alpha_c} \frac{\alpha_m M_m C_c - \alpha_c M_c C_m}{r_c K_c^{\text{sat}} C_m + r_m K_m^{\text{sat}} C_c} \left(\frac{\alpha_c M_c}{C_c} - \frac{\alpha_m M_m}{C_m} \right) \left(2 + \frac{h_c C_c}{L_c} \right), \quad (6)$$

where $G^{\text{low}} = -1/2(h_c D_m \kappa_c / h_m D_c \kappa_m + 1)$. When the fracture is infinitely thin but remains a nonzero value (i.e., $h_c \rightarrow 0$ but $h_c \neq 0$), the fracture does not have a pore structure and is hollow ($\phi_c \rightarrow 1$, $\zeta_c^{\text{uni}} \approx 1$, $\alpha_c \rightarrow 1$), and $h_c C_c / L_c \ll 2$. The limits $M_c \rightarrow C_c$ and $\alpha_c M_c / C_c \rightarrow 1$ exist as $h_c \rightarrow 0$ (Brajanovski et al. 2005). Therefore, we can obtain as follows:

$$Z_n^{\text{low}} = \frac{r_c}{M_c} (\alpha_m M_m - C_m)^2 \frac{H}{\frac{r_c}{L_c} L_m M_m K_m^{\text{sat}} + r_m K_m^{\text{sat}} C_m}. \quad (7)$$

Besides the specific parameters in Eq. (7), Z_n^{low}/H has the same form compared to the second part (i.e., the fracture compliance) of Eq. (18) in Brajanovski et al. (2005). Note that the fracture thickness in Eq. (7) for DFCM has a nonzero value, even though $h_c \rightarrow 0$. Equation (7) can be rewritten with the same defined parameters as given by Eq. (18) in Brajanovski et al. (2005) if one takes the limit $Z_n^{\text{dry}} = h_c / L_c$ as $L_c \rightarrow 0$ when $h_c \rightarrow 0$. We can see that the normal compliance of fractures is proportional to the fracture spacing (H) for a fixed fracture thickness fraction (r_c) (Eq. 7). However, the effective elastic modulus of P-wave is independent of the fracture spacing (H) from Eqs. (5) and (7). The comparison between two models for the case of an oil-saturated fractured rock (the Lamé constants used in this comparison are cited from Part I) shows that there is a good agreement between the DFCM and Brajanovski's model over the entire frequency range, just as shown in Fig. 1. It is shown that the fracture compliance calculated by DFCM (Eq. 1) is slightly less than that of the Brajanovski's model (Eq. 13 in Brajanovski et al. 2005), and these two models are completely consistent with each other, as $\omega \rightarrow \infty$ or $h_c \rightarrow 0$.

These two theoretical models (DFCM and Brajanovski's model) are also compared in a full frequency regime by considering P-wave velocities in

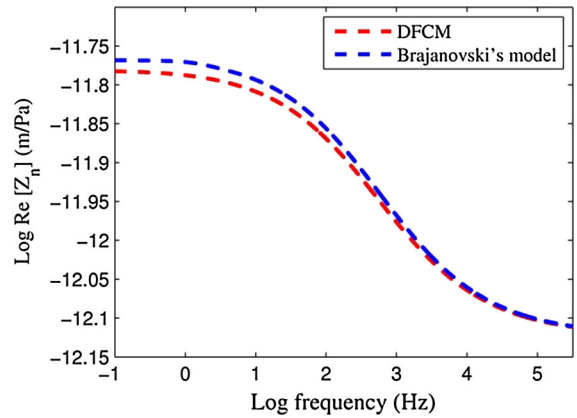


Figure 1

Differences of the normal fracture compliances between the DFCM and Brajanovski's model for an oil-filled fracture with $\phi_m = 0.12$, $\phi_c = 0.48$, $H = 1.5$ m, and $r_c = 0.003$

a direction perpendicular to the aligned fractures. To compute the wave velocities of the fractured medium, the fracture compliances are used to derive the effective elastic moduli of the fractured medium. The relationships between compliances and stiffness matrix are given in Appendix. The assumption underlying this relationship is that the wavelength is much larger than the fracture scale (e.g., fracture size or spacing). Figure 2 shows that the deviations between the two models are acceptable ($\leq 0.5\%$) and are frequency-dependent for different petrophysical parameters. Figure 2a shows that the difference between the two models increases with an increasing fracture thickness. The main reason is that the displacement across a fracture in DFCM is discontinuous, while the stress is continuous based on the linear slip theory. The P-wave velocity calculated by DFCM is less than that by Brajanovski's model as the high-frequency part of the effective modulus in the latter is computed by the weighted harmonic average of the saturated moduli of the host rock and fractures, and this deviation increases with increasing wave frequency. For instance, at the high-frequency limit, the effective modulus in Brajanovski's model is $1/C_{\text{eff}}^{\text{vert}} = (1 - r_c)/C_m + r_c/C_c$, while, in the DFCM, the modulus is given by $1/C_{\text{eff}}^{\text{vert}} = 1/C_m + r_c/C_c$. As has been discussed, the increasing fracture thickness has a similar effect as that of increasing wave frequency, by a factor $h_c \sqrt{i\omega/D_c}$ (the ratio of characteristic size to

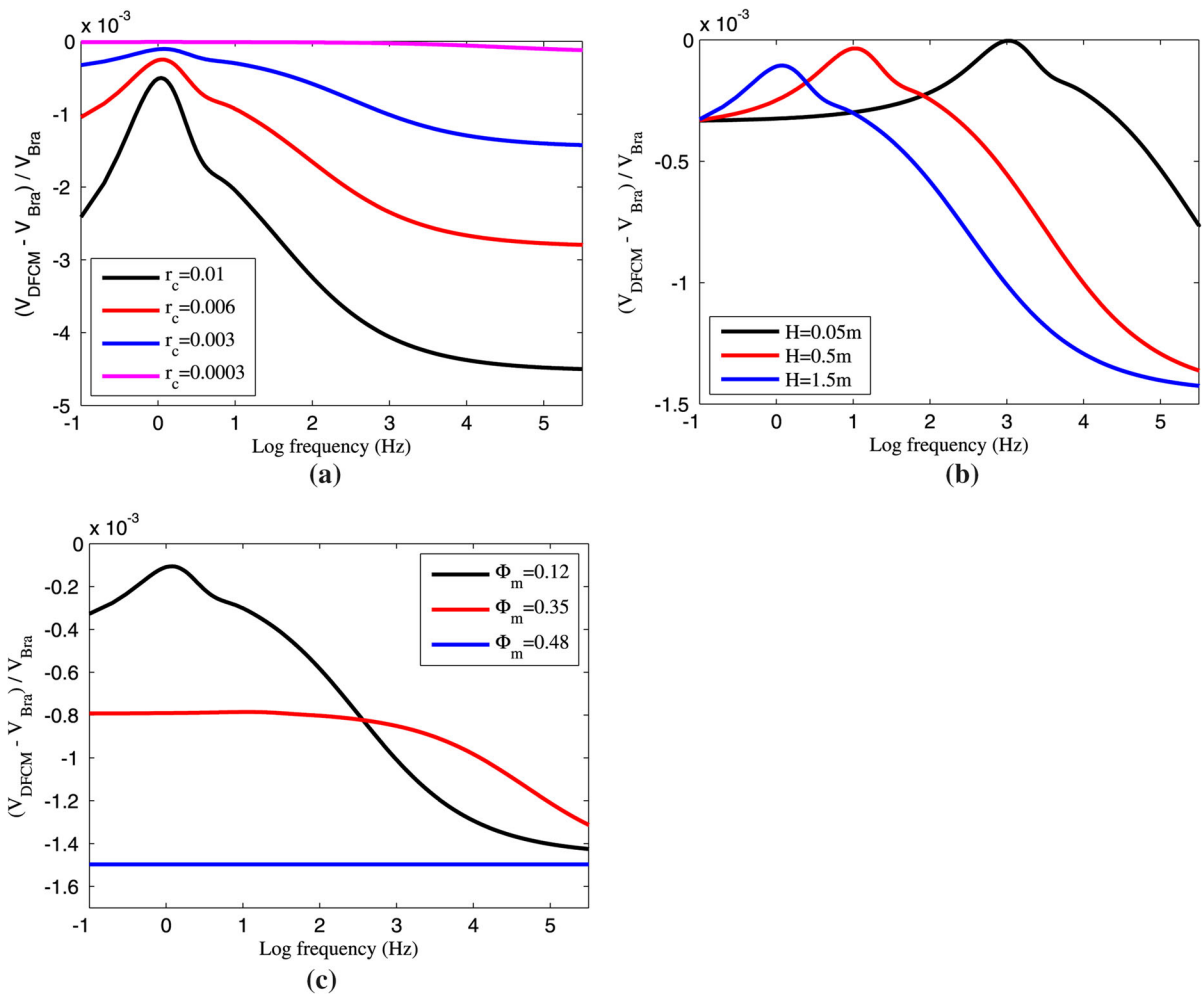


Figure 2

Differences of the vertical P-wave velocities between the DFCM and Brajanovski's model as a function of frequency with (a) different fracture thicknesses: $\phi_m = 0.12$, $\phi_c = 0.48$, $H = 1.5$ m; (b) different fracture spacing: $\phi_m = 0.12$, $\phi_c = 0.48$, $r_c = 0.003$; and (c) different host porosities: $H = 1.5$ m, $\phi_c = 0.48$, and $r_c = 0.003$

diffusion length) in Eq. (1). On the other hand, the two models exhibit a similar frequency dependence as is shown in Fig. 2b, and the characteristic frequency of the velocity deviation curve tends to the low-frequency range with an increasing fracture spacing. The difference between the two models increases with an increasing porosity of the host rock (Fig. 2c). It is caused by the fact that the WIFF effect is gradually weakened and the role of the rock matrix is enhanced by the increase of ϕ_m . When $\phi_m \rightarrow \phi_c$, the fractured rock becomes a homogeneous porous medium and the effects of fractures vanish. The

WIFF disappears and the effective elastic modulus is equivalent to the results of the high-frequency limit.

3. Experimental Comparison Results

To verify the DFCM and other theoretical models, a reasonable manufacturing and measurement workflow for synthetic specimens is required to guarantee that the pore structure of synthetic specimens is close to that of natural rocks and matches that of theoretical models (Ding et al. 2014, 2017), i.e., these synthetic

Table 1
Physical parameters of two synthetic specimens

Variable	Value	SI unit
$K_1^{\text{dry}}, \mu_1^{\text{dry}}$	12.4, 7.61	GPa
$K_2^{\text{dry}}, \mu_2^{\text{dry}}$	12.7, 7.02	GPa
H_1, H_2, h_c	0.0031, 0.0025, 0.00006	m
α_1, α_2	0.8169, 0.8792	–
ϕ_{m1}, ϕ_{m2}	0.41, 0.44	–
r_1, r_2	0.002, 0.0015	m
e_1, e_2	0.60, 0.68	–
$\rho_1^{\text{dry}}, \rho_1^{\text{sat}}, \rho_2^{\text{dry}}, \rho_2^{\text{sat}}$	1456, 1872, 1424, 1869	kg/m ³

rocks should not only embed the pores and fractures, but should also allow fluids to flow between the fractures and the connected pores when waves propagate through the specimens. This suggests that the WIFF process at the local fracture scale is an important dispersion and attenuation mechanism. Meanwhile, we need to estimate the selected physical and geometrical parameters of the pores and fractures during the specimens manufacturing process. In other words, we guarantee that the theoretical characteristic frequencies of squirt flow (Wang et al. 2017; Chapman 2003) calculated using the selected physical parameters of specimens (Table 1) are not at the low- or high-frequency limits relative to the laboratory testing frequency.

3.1. Synthetic Rock Specimens and Experimental Measurements

Ultrasonic wave velocity measurements in octagonal-shaped synthetic fractured rock specimens are utilized in this study, based on a new manufacturing method shown in Fig. 3a (Ding et al. 2014). This method not only can produce samples whose mineral compositions and cementations are similar to natural rocks, but it allows for producing synthetic sandstones containing controlled fracture density and geometrical distribution. The epoxy discs (fractures) are located within the same plane on the surface of each layer and surrounded by a sand mixture (host medium) during the manufacture process. Then, the samples are left to dry at a constant temperature in an oven for several weeks. Finally, the samples are sintered in a furnace and the high molecular (epoxy) discs are decomposed and drained out, leaving flat cavities simulating fractures.

P, SH (S1) and SV (S2) wave velocities are measured in these synthetic sandstones at the incidence angle of 0° (perpendicular to the fractures), 45°, 90° (parallel to fractures), and 135° using an ultrasonic measurement system with 0.5 MHz transducers at full-water saturation and at different fracture densities. The main elastic parameters of the matrix and fractures of the two synthetic specimens are shown in Table 1. Besides the parameters of fractures, all physical parameters of the background matrix in Table 1 are obtained from a reference specimen manufactured without fractures. This reference specimen has the same pore structure as the matrix of fractured synthetic specimens. The 1D fracture number densities at normal direction of the two specimens are 400 and 500/m, and the corresponding volume densities are 0.0486 and 0.0665 calculated by na^3/V , where n is the total fracture number of a rock specimen, a is the radius of fractures, and V is the volume of this rock specimen.

The DFCM is derived using the first-order compliance method, and the contribution of fracture interactions to the effective elastic tensor is assumed negligible. This assumption is supported by the results obtained by Grecheka and Kachanov (2006) for crack densities lower than 0.1. The fracture densities of synthetic rocks are less than 0.1, as shown in Table 1; therefore, the basic assumption of linear behavior of DFCM and Hudson's first-order model can be fully satisfied at the fracture densities of the specimens.

3.2. WIFF in Synthetic Sandstone Specimens

Figure 3b is the fracture distribution diagram of the synthetic specimens. In the normal direction, fractures are simulated by a set of parallel discs. The fracture network is designed in accordance with the geometrical and mechanical properties used for the wave-induced fluid flow in the DFCM. The WIFF mainly occurs around the disc-shaped fractures, while pore fluid in the rest of the sample remains essentially unperturbed.

The DCFM and other existing theoretical models require the knowledge of the permeability of the host rock and that of the fractures. Permeability of the fractures and host rock in the DFCM is given by

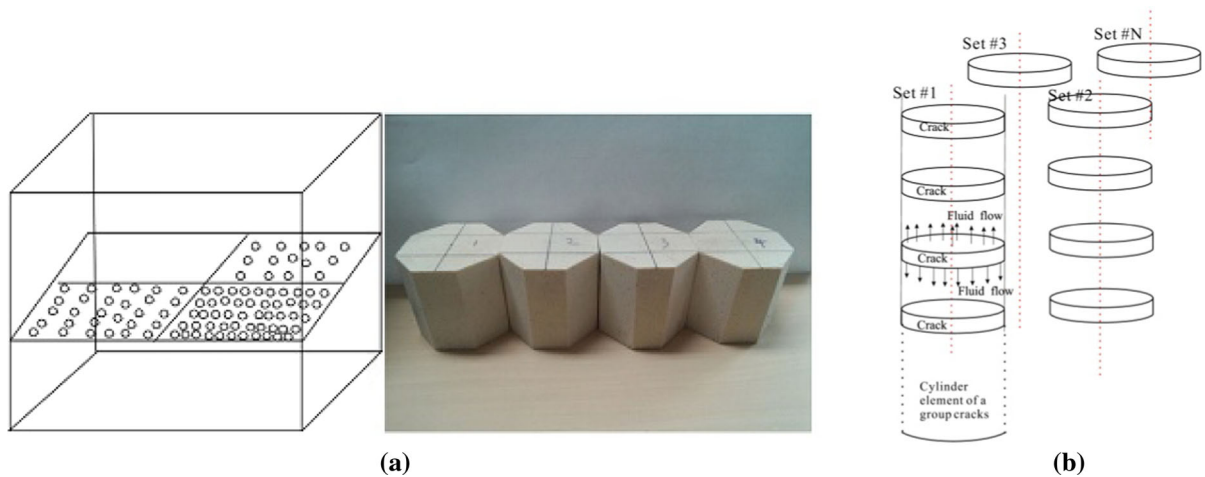


Figure 3

a Synthetic rock specimens with the parallel-aligned penny-shaped fractures. **b** Fracture spatial distribution in the synthetic rocks in the normal direction

$\kappa = \beta \ell^2 \phi^3 / (1 - \phi)^2$ based on the Kozeny–Carman equation (Bear 1972; Mavko et al. 1998). The permeability of the host matrix is still calculated by this empirical equation, because the test frequency is much lower than the Biot’s characteristic frequency computed from Table 1. However, since the fractures in the synthetic specimens are non-porous ($\phi_c = 1$), the permeability within the fractures cannot be described by the Kozeny–Carman equation. Navier–Stokes equation is an alternative to analyze the fluid flow in these non-porous fractures in the normal direction. We use the specific permeability of the circular fractures to compute wave responses by the DFCM corresponding to the specimens’ parameters. We assume that viscous fluid flow in a penny-shaped fracture in the normal direction satisfies the viscous laminar flow condition. According to the viscous fluid mechanics, the permeability of circular fractures in the normal direction is as follows (Wang and Zhang 2014):

$$\kappa_j(\omega) = -\frac{\eta}{i\omega\rho_f} \left\{ 1 - \frac{2J_1 \left[r_j \left(\frac{-i\omega\rho_f}{\eta} \right)^{\frac{1}{2}} \right]}{r_j \left(\frac{-i\omega\rho_f}{\eta} \right)^{\frac{1}{2}} J_0 \left[r_j \left(\frac{-i\omega\rho_f}{\eta} \right)^{\frac{1}{2}} \right]} \right\}, \tag{8}$$

where r_j is the fracture radius, ρ_f is the density of water, η is the viscosity of water, and J_0 and J_1 are the zero- and first-order Bessel functions,

respectively. Indexes $j = 1, 2$ denote the two different rock specimens, and they have the same definitions in this paper. Equation (8) describes the wave-induced average flux within fractures in the normal direction. When $\omega \rightarrow 0$, $\kappa_j(0) = r_j^2 / 8$, which is equivalent to the permeability of a penny-shaped fracture corresponding to Poiseuille flow. In contrast, when $\omega \rightarrow \infty$, $\kappa_j(\infty) \rightarrow 0$, where the skin depth within fractures tends to zero and the fluid cannot flow within a wave oscillation period. The WIFF in synthetic specimens satisfies the basic assumptions of the fluid diffusion equations of the DFCM for periodic aligned fractures. To calculate the velocities for the synthetic specimens, according to the definition of the effective stiffness for fractured media presented by Liu et al. (2000), the theoretical total effective stiffness of the synthetic specimens can be derived as the area weighted average $C_j^{\text{tot}} = (1 - e_j)C_0 + e_jC_j$ (C_j is the effective stiffness of a single cylinder element based on the DFCM and is derived in Appendix on the basis of the relation between the stiffness matrix and the compliance matrix), where e_j is the fracture surface density (the total surface area of fractures in a layer divided by the total layer area) of the j th specimen of each fractured layer (e_j is invariable for each fractured layer within a rock specimen); and C_0 is the elastic matrix of the saturated host medium, which can be computed by Gassmann’s equation (Gassmann 1951). Then, using Christoffel’s equations, the

velocity and attenuation characteristics of elastic waves are obtained.

3.3. Scale Correlations of the DFCM with Discrete Fractures Model

In the DFCM, the WIFF process between the more compliant layers and stiffer layers in a sequence of periodic poroelastic layers is considered, and the compliant layer models a fracture with an infinite radius, parameterized with different physical properties in comparison with the host poroelastic medium (stiffer layer). However, the fractures in the synthetic rocks are discrete and have a finite dimension. Now, we discuss how the effects of fracture parameters of the synthetic rocks are considered in the DFCM.

A key parameter in the synthetic rocks is the aspect ratio of the fractures. Fractures in the synthetic rocks have a small and finite aspect ratio (Table 1), while the aspect ratio of fractures in the DFCM is infinitely small (≈ 0). According to the diffusion equation, the WIFF depends on the initial pressure difference and the permeability of the porous medium. Equation $P_c^0 = \zeta_c^{\text{uni}} \sigma_n$ was used to obtain the fractures' instantaneous (undrained) initial pressure (Norris 1993; Wang 2000; Wang et al. 2017), where σ_n is the stress normal to the fracture surface. Therefore, the induced pore pressure within fractures is equivalent to the uniaxial stress wave if the fractures have a large porosity ($\alpha_c = 1$, $M_c = C_c = K_f$, and $\zeta_c^{\text{uni}} = 1$). However, this relationship is not applicable for the small-scale fractures with a finite aspect ratio. Therefore, the instantaneous pressure induced in penny-shaped fractures needs to be reconsidered based on the equation $P_c^0 = \zeta_c^{\text{uni}} \sigma_n$ (Zatsepin and Crampin 1997; Chapman 2003), where $\zeta_c^{\text{uni}} = K_f / [K_f + \pi \mu \gamma / 2(1 - \nu)]$, ν and μ are the Poisson's ratio and shear modulus of the matrix material, respectively, and γ is the aspect ratio. This formula implies that a fracture with a small aspect ratio can be compressed and deformed easily. It can be obtained as $\zeta_c^{\text{uni}} \rightarrow 1$, when $\gamma \rightarrow 0$ (e.g., the infinite flat fractures). In the DFCM, the fracture-related ζ_c^{uni} is used to analyze the effects of aspect ratio on WIFF and calculate wave propagation velocities, when we compare the theoretical results with the experimental data.

In addition to the wave-induced pressure in the fractures, the aspect ratio of the fractures also influences the subsequent fluid flow process. The previous models have used Darcy's law to analyze the fluid exchange between fractures and the pores in the host medium (Jakobsen et al. 2003; Chapman et al. 2002; Chapman 2003), and the corresponding equation is given by the following:

$$Q = \frac{(P_c - P_m)}{b} \kappa \frac{\pi a^2}{\eta}, \quad (9)$$

where a is the fracture radius, b is half the fracture thickness, and κ is the permeability of the host rock. The effects of aspect ratio are incorporated into Eq. (9). The influence of aspect ratio of the fractures of the synthetic rocks is also taken into account by the DFCM during the WIFF process. The parameter b in Eq. (9) is hidden in Eq. (1) and corresponds to the fracture thickness and spacing in the DFCM, while the effects of parameter a in Eq. (9) are considered when we calculating the effective elastic moduli of the synthetic rocks (Liu et al. 2000; Chapman 2003). First, for each layer including fractures, the effective moduli can be derived as $C_{\text{eff}} = C_0 - e C_{\text{fra}}$ (Liu et al. 2000), where e is the fracture surface density (related to the parameter a) and C_{fra} is the first-order excess stiffness correction of the individual fracture. On the other hand, the total effective stiffness is given by $C_j^{\text{tot}} = (1 - e_j) C_0 + e_j C_j$ for the fractures spatial distribution as is shown in Fig. 3b. For a set of fractures, the fracture surface density is $e = 1$ and $C_j = C_{\text{eff}}$ based on Liu's equation (Liu et al. 2000). Therefore, the total effective stiffness of the j th rock specimen can be rewritten as $C_j^{\text{tot}}(1 - e_j) C_0 + e_j(C_0 - C_{\text{fra}})$, and then, it is transformed into the expression $C_j^{\text{tot}} = C_0 - e_j C_{\text{fra}}$, which is consistent with the previous definition (Liu et al. 2000).

3.4. Comparisons Between Theoretical Model and Experimental Results

Figure 4 shows that velocity anisotropy (velocity variation with angle) is significant for the two water-saturated specimens. The highest P-wave velocity can be measured at an incidence angle of 90° and the lowest at 0° , normal to the fractures. It is qualitatively consistent with the anisotropy interpreted from multi-

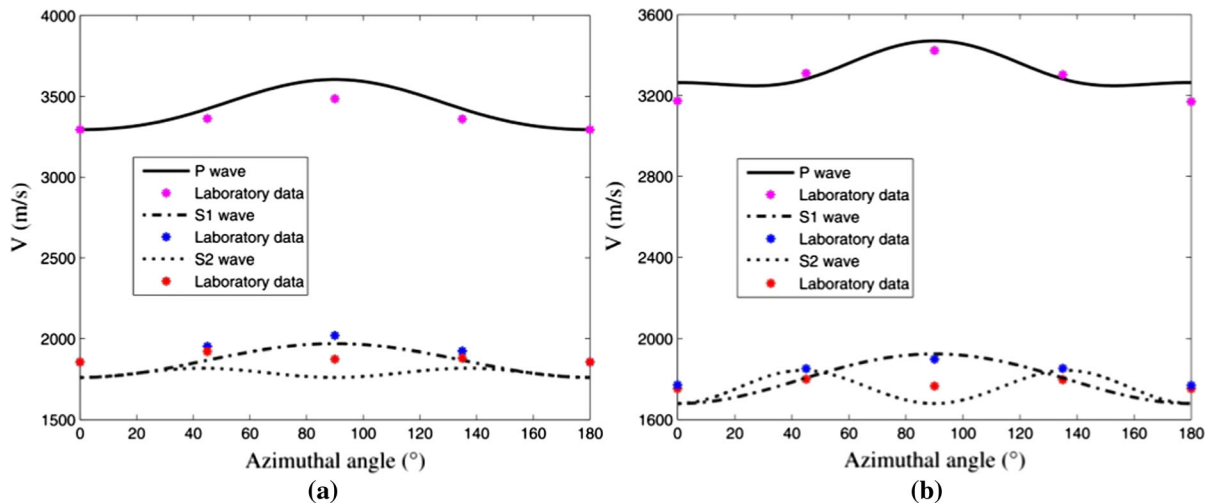


Figure 4

Comparisons between the measured data and the complex fracture compliance model: **a** synthetic rock 1 and **b** synthetic rock 2

azimuth P-wave data (Hall and Kendall 2003; Maultzsch et al. 2007). The S1-wave (i.e., the fast shear-wave, with a polarization parallel to the fractures) velocity shows variation similar to that of the P-wave velocity, while a maximum of S2-wave (i.e., slow shear-wave, with a polarization normal to fracture planes) velocity occurs at 45°. The shear-wave splitting (SWS) theory is considered, which is expressed as the parameter $SWS (\%) = 100 \times (V_{S1} - V_{S2})$. The value of SWS is an indicator of the fracture characteristics (Crampin 1985; Verdon and Kendall 2011). The polarization of the fast S-wave can be the indicator of the fracture directions and the SWS is a measure of the magnitude of fracture-induced anisotropy.

The experimental data agree well with the theoretical velocities. For an incidence orthogonal to the fractures, the difference between the measured P-wave velocities and the corresponding theoretical results is smaller than that of the S-wave velocities. This is due to the effects of the WIFF that are most significant for P-waves across fractures in the normal direction. On the other hand, the WIFF process vanishes for the S-waves in this direction. In contrast, the S-wave velocities calculated by the theoretical model are closer to the experimental values than the P-wave velocities, for an incidence parallel to the fractures. The fast S-wave (S1-wave) is equivalent to the slow S-wave (S2-wave) as the same polarization

at 90° direction. To estimate the significance of the effects of WIFF, the theoretical results are also compared with Hudson's high-frequency model (Fig. 5). Hudson's original model is a high-frequency approximation with respect to the WIFF process (Hudson 1981). It ignores the fluid exchange between the fractures and the pores when elastic waves propagation through the rocks. As shown in Fig. 5, P-wave velocities from the DFCM are relatively more accurate than Hudson's model in relation to the laboratory data, especially perpendicular to the fracture planes because of the WIFF process. An equation for error analysis is presented to thoroughly estimate the agreement between the theoretical models and laboratory data. We use the root-mean-square error (RMSE) equation $\text{Error} = \sqrt{\sum_{i=1}^5 (V_{\text{lab}} - V_{\text{model}})_i^2 / 5}$ (where i denotes the i th testing angle) to decide which model exhibits better fit to the laboratory data. It is evidently observed that in Fig. 5, the P- and S2-waves are more accurate by the DFCM, and these waves have the smaller square errors (RMSE of P-wave are 62.72 and 139.79 m/s from the DFCM and Hudson's model, respectively; RMSE of S2-wave are 65.92 and 95.97 m/s from the DFCM and Hudson's model, respectively). The effects of local fluid flow on these waves are more important than the S2-wave. On the other hand, S2-wave from Hudson's model has a relatively accurate

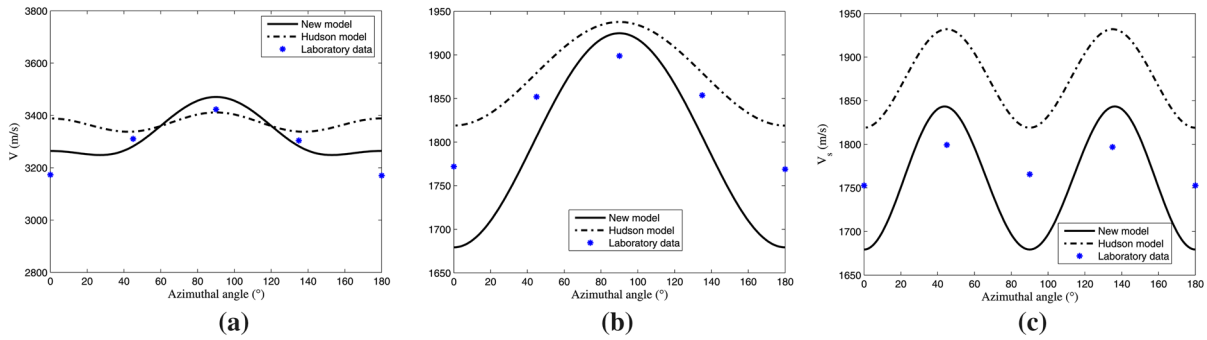


Figure 5

Comparisons between Hudson's high-frequency model and the complex fracture compliance model, using the parameters of synthetic rock 2: **a** P-wave; **b** S1-wave; **c** S2-wave

results compared with the results calculated using the DFCM. Almost all velocities based on Hudson's model are higher than the DFCM, because the fluid in fractures is isolated (and un-relaxed) in Hudson's model. We anticipate that the dynamic fracture compliance model will approach Hudson's model at the high-frequency limit.

Although the experimental testing frequency is in the ultrasonic band, the DFCM is appropriate for explaining the experimental data, as shown in Fig. 4. The permeability of the synthetic rocks is about 170 mD, and the characteristic frequency of the synthetic rocks can be estimated by Wang et al. (2017) or Chapman (2003) using the parameters in Table 1. From Appendix in Part I (Wang et al. 2017), these characteristic frequencies of the synthetic rocks corresponding to squirt flow are given by $\omega_c = 4\sqrt{2}D_c/h_c^2(1 + \kappa_c\sqrt{D_m}/\kappa_m\sqrt{D_c})$ and are about 0.6 MHz, which has the same frequency range as the testing frequency. It means that the WIFF process is an important mechanism for wave propagation in fractured rocks. Overall, this shows that the DFCM yields better agreements with the laboratory observations (Fig. 5) than the high-frequency model (Hudson's model).

3.5. Comparisons Between Theoretical Models at the Low-Frequency Limit

The dynamic fracture compliance model is frequency-dependent, and it is also valid at the low-frequency limit. Figure 6 shows the comparison

between DFCM and Thomsen's low-frequency model (Thomsen 1995), which also considers the exchange of fluid between pores and fractures. Using the parameters (e.g., the porosity and fracture radius) of the synthetic rocks in Table 1, the results of the DFCM agree well with Thomsen's low-frequency model for all waves. Furthermore, the results from the DFCM are slightly lower than Thomsen's results as a assumption that the porosity of the host medium was restricted in a relatively low region ($< 10\%$) in Thomsen's original model (Thomsen 1995). Obviously, the porosity of the synthetic rocks exceeds this porosity range (see Table 1). As shown in Figs. 5c and 6b, the S1-wave is frequency-independent, since particle oscillates parallel to the fracture surfaces (a pure shear oscillation will not compress the fractures), and as such no WIFF occurs.

4. Discussion

Scattering and intrinsic attenuation mechanisms are the two main wave loss mechanisms for heterogeneous porous media fully saturated with a single fluid (Sarout 2012; Wang et al. 2016). Besides the intrinsic anelasticity due to WIFF, the scattering effects should also be considered, in the case that the ratio of fracture radius to wavelength is about 0.3 for the two synthetic rocks (Smyshlyaev et al. 1993; Hudson et al. 2001). However, the experimental results are still helpful for the qualitative validation of the dynamic fracture compliance model, since the

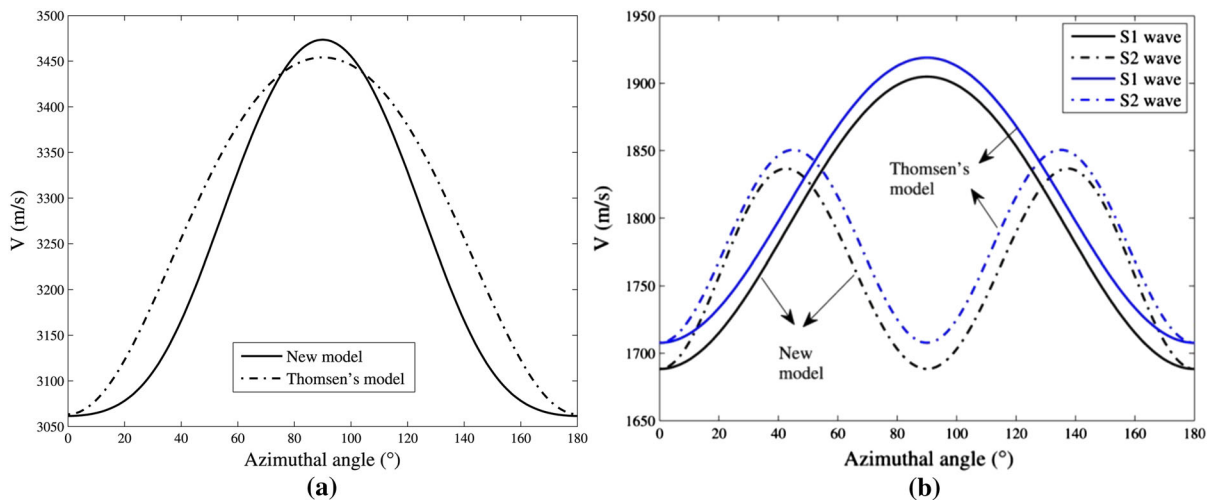


Figure 6

Comparisons between the Thomsen's low-frequency model and the complex fracture compliance model, using the parameters of synthetic rock 2: **a** P-wave; **b** S-wave

fracture density in the two synthetic rocks is very low (<0.1), and the interactions between fractures are weak. Several useful correlations were performed by Tillotson et al. (2014) between experimental data and theoretical models, which suggest that the model predictions are relatively unaffected by scattering. Smyshlyaev et al. (1993) extended the self-consistent method to calculate wave velocity in media containing aligned circular fractures with a volume density $e = 0.1$ and for an incidence angle of 45° to the normal direction. The phase velocity in this model has a deviation of around 3% from the estimate value at the long wavelength approximation. The experimental results of the two specimens support the methodology of the dynamic fracture compliance model. The results of the model agree better with the experimental data as compared to Hudson's model. The significance of WIFF in a fractured porous medium plays a dominant role in explaining the observed wave anelasticity characteristics rather than the mechanism of scattering in the models considered here

The effective moduli of a fractured porous medium are dependent on the incidence angle relative to the direction normal to the fracture interfaces. The discrepancies between the experimental data and theoretical results in the direction perpendicular to the fractures are less than those in the direction parallel to the fractures. For these flat fractures, fluid

flow only depends on the stress variations perpendicular to the fracture surface. The normal component of plane-wave stress along its propagation path was provided by White (1983).

5. Conclusions

The theoretical model of dynamic fracture compliance presented in the companion paper (Part I) is compared with other model published in the literature and the experimental data on synthetic rocks specimens. In the examples of numerical comparison, the DFCM gives a good agreement with Brajanovshi's model with different fracture and rock parameters in a full frequency regime. In the experimental comparative analysis, two synthetic specimens fully saturated with water have the similar mineral components and pore structures to natural rocks. The geometrical and physical parameters of fractures and pores can be controlled during the specimens manufacturing process. The results based on the DFCM are appropriate for explaining the experimental data. The characteristic frequency of squirt flow in the synthetic specimens is close to the testing frequency, and therefore, the range of ultrasonic testing frequency cannot be simply treated as the high-frequency limit. It is essential to consider the effects of WIFF on the

analysis of laboratory data. Overall speaking, the DFCM is in better agreement with the experimental data than Hudson’s high-frequency (un-relaxed) model.

This paper focuses on the accuracy of analytical solutions of the dynamic fracture compliance model. Although the comparison with laboratory data is performed in the ultrasonic frequency range, it is still reasonable to believe that the DFCM is applicable for characterizing the fractured porous reservoirs in nature. Further investigations are required on the issues about the more complex fracture systems and different saturation patterns, e.g., multiple fracture sets and partial saturation.

Acknowledgements

This work is financially supported by the ‘‘Distinguished Professor Program of Jiangsu Province, China’’, the open fund of the State Key Laboratory of the Institute of Geology and Geophysics, CAS (SKLGED2017-5-2E), and the open fund of SINOPEC Key Laboratory of Geophysics. The authors thank Joel Sarout and Yves Gueguen for the helpful comments.

Appendix

Effective Elastic Moduli of a Fractured Medium

By taking φ as the angle between the direction normal to paralleled fractures and the coordinate system Y_1 -axis (as shown in Fig. 7), the matrix of fracture compliance (Eq. 10) can be given in the observing coordinate system based on the Band’s conversion (Liu et al. 2006; Winterstein 1990). When $\varphi = 0^\circ$, the off-diagonal terms of the compliance matrix are zero:

$$\bar{S}^f = \begin{bmatrix} \bar{S}_{11}^f & \bar{S}_{12}^f & 0 & 0 & 0 & \bar{S}_{16}^f \\ & \bar{S}_{22}^f & 0 & 0 & 0 & \bar{S}_{26}^f \\ & & 0 & \frac{0}{S_{44}^f} & \frac{0}{S_{45}^f} & 0 \\ & & & \bar{S}_{44}^f & \bar{S}_{45}^f & 0 \\ & & & & \bar{S}_{55}^f & 0 \\ & & & & & \bar{S}_{66}^f \end{bmatrix}, \quad (10)$$

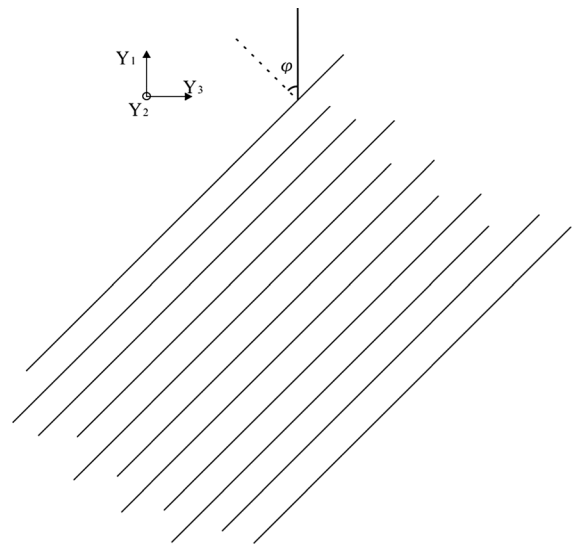


Figure 7
Diagram of paralleled fractures in the observing coordinate system

where

$$\bar{S}_{11}^f = \frac{3Z_n + Z_t}{8} + \frac{Z_n \cos(2\varphi)}{2} + \frac{(Z_n - Z_t) \cos(4\varphi)}{8} \quad (11)$$

$$\bar{S}_{22}^f = \frac{3Z_n + Z_t}{8} - \frac{Z_n \cos(2\varphi)}{2} + \frac{(Z_n - Z_t) \cos(4\varphi)}{8} \quad (12)$$

$$\bar{S}_{44}^f = \frac{Z_t [1 - \cos(2\varphi)]}{2} \quad (13)$$

$$\bar{S}_{55}^f = \frac{Z_t [1 + \cos(2\varphi)]}{2} \quad (14)$$

$$\bar{S}_{66}^f = \frac{Z_n + Z_t}{2} - \frac{(Z_n - Z_t) \cos(4\varphi)}{2} \quad (15)$$

$$\bar{S}_{12}^f = \frac{(Z_n - Z_t) [1 - \cos(4\varphi)]}{8} \quad (16)$$

$$\bar{S}_{16}^f = \frac{Z_n \sin(2\varphi)}{2} + \frac{(Z_n - Z_t) \sin(4\varphi)}{4} \quad (17)$$

$$\bar{S}_{26}^f = \frac{Z_n \sin(2\varphi)}{2} - \frac{(Z_n - Z_t) \sin(4\varphi)}{8} \quad (18)$$

$$\bar{S}_{45}^f = \frac{Z_t \sin(2\varphi)}{2}. \quad (19)$$

The host porous medium is isotropic and homogeneous, and the corresponding compliance is given by the following:

$$S_0 = \begin{bmatrix} \frac{1}{E} & \frac{-\nu}{E} & \frac{-\nu}{E} & 0 & 0 & 0 \\ & \frac{1}{E} & \frac{-\nu}{E} & 0 & 0 & 0 \\ & & \frac{1}{E} & 0 & 0 & 0 \\ & & & \frac{1}{\mu} & 0 & 0 \\ & & & & \frac{1}{\mu} & 0 \\ & & & & & \frac{1}{\mu} \end{bmatrix}, \quad (20)$$

E , ν , and μ are the Young modulus, Poisson ratio, and shear modulus of the saturated host frame, according to the Gassmann's equations (Gassmann 1951), respectively. Then, the effective compliance of the fractured medium is derived as follows:

$$S = S^0 + \frac{\bar{S}^f}{H}. \quad (21)$$

The effective elastic stiffness matrix of a fractured medium is as follows:

$$C = S^{-1}, \quad (22)$$

where

$$C_{11} = \frac{S_{22}S_{33}S_{66} - S_{26}^2S_{33} - S_{23}^2S_{66}}{Q} \quad (23)$$

$$C_{12} = \frac{S_{13}S_{23}S_{66} + S_{16}S_{26}S_{33} - S_{12}S_{33}S_{66}}{Q} \quad (24)$$

$$C_{13} = \frac{S_{26}^2S_{13} + S_{12}S_{23}S_{66} - S_{13}S_{22}S_{66} - S_{16}S_{23}S_{26}}{Q} \quad (25)$$

$$C_{16} = \frac{S_{23}^2S_{16} + S_{12}S_{26}S_{33} - S_{13}S_{23}S_{26} - S_{16}S_{22}S_{33}}{Q} \quad (26)$$

$$C_{22} = \frac{S_{11}S_{33}S_{66} - S_{16}^2S_{33} - S_{13}^2S_{66}}{Q} \quad (27)$$

$$C_{23} = \frac{S_{16}^2S_{23} + S_{12}S_{13}S_{66} - S_{11}S_{23}S_{66} - S_{13}S_{16}S_{26}}{Q} \quad (28)$$

$$C_{26} = \frac{S_{13}^2S_{26} + S_{12}S_{16}S_{33} - S_{11}S_{26}S_{33} - S_{13}S_{16}S_{23}}{Q} \quad (29)$$

$$C_{33} = \frac{S_{11}S_{22}S_{66} + 2S_{12}S_{16}S_{26} - S_{12}^2S_{66} - S_{16}^2S_{22} - S_{26}^2S_{11}}{Q} \quad (30)$$

$$C_{36} = \frac{S_{11}S_{23}S_{26} + S_{13}S_{16}S_{22} - S_{12}S_{13}S_{26} - S_{12}S_{16}S_{23}}{Q} \quad (31)$$

$$C_{44} = \frac{S_{55}}{S_{44}S_{55} - S_{45}^2} \quad (32)$$

$$C_{45} = \frac{-S_{45}}{S_{44}S_{55} - S_{45}^2} \quad (33)$$

$$C_{55} = \frac{S_{44}}{S_{44}S_{55} - S_{45}^2} \quad (34)$$

$$C_{66} = \frac{S_{11}S_{22}S_{33} + 2S_{12}S_{13}S_{23} - S_{12}^2S_{33} - S_{13}^2S_{22} - S_{23}^2S_{11}}{Q} \quad (35)$$

$$Q = 2(S_{12}S_{16}S_{26}S_{33} + S_{12}S_{13}S_{23}S_{66} - S_{13}S_{16}S_{23}S_{26}) \\ + S_{11}S_{22}S_{33}S_{66} + S_{13}^2S_{26}^2 + S_{16}^2S_{23}^2 - S_{12}^2S_{33}S_{66} \quad (36)$$

REFERENCES

- Ass'ad, J. M., Tatham, R. H., & McDonald, J. A. (1992). A physical model study of microcrack-induced anisotropy. *Geophysics*, 57(12), 1562–1570.
- Ba, J., Xu, W., Fu, L. Y., Carcione, J. M., & Zhang, L. (2017). Rock anelasticity due to patchy saturation and fabric heterogeneity: A double double-porosity model of wave propagation. *Journal of Geophysical Research*, 122(3), 1949–1976.
- Ba, J., Zhao, J., Carcione, J. M., & Huang, X. X. (2016). Compressional wave dispersion due to rock matrix stiffening by clay squirt flow. *Geophysical Research Letters*, 43(12), 6186–6195.
- Bear, J. (1972). *Dynamics of fluid in porous media*. New York: Elsevier.
- Biot, M. A. (1956). Theory of propagation of elastic waves in a fluid-saturated porous solid. I. Low-frequency range. *The Journal of the Acoustical Society of America*, 28(2), 168–178.
- Biot, M. A., & Willis, D. G. (1957). The elastic coefficients of the theory of consolidation. *Journal of Applied Mechanics*, 24, 594–601.
- Brajanovski, M., Gurevich, B., & Schoenberg, M. (2005). A model for P-wave attenuation and dispersion in a porous medium permeated by aligned fractures. *Geophysical Journal International*, 163(1), 372–384.
- Carcione, J. M., Picotti, S., & Santos, J. E. (2012). Numerical experiments of fracture-induced velocity and attenuation anisotropy. *Geophysical Journal International*, 191(3), 1179–1191.
- Chapman, M., Zatsepin, S. V., & Crampin, S. (2002). Derivation of a microstructural poroelastic model. *Geophysical Journal International*, 151(2), 427–451.

- Chapman, M. (2003). Frequency-dependent anisotropy due to meso-scale fractures in the presence of equant porosity. *Geophysical Prospecting*, 51(5), 369–379.
- Crampin, S. (1985). Evaluation of anisotropy by shear-wave splitting. *Geophysics*, 50(1), 142–152.
- de Figueiredo, J., Schleicher, J., Stewart, R. R., Dayur, N., Omoboya, B., Wiley, R., et al. (2013). Shear wave anisotropy from aligned inclusions: ultrasonic frequency dependence of velocity and attenuation. *Geophysical Journal International*, 193(1), 475–488.
- Ding, P., Di, B., Wang, D., Wei, J., & Li, X. (2014). P and S wave anisotropy in fractured media: Experimental research using synthetic samples. *Journal of Applied Geophysics*, 109, 1–6.
- Ding, P., Di, B., Wang, D., Wei, J., & Li, X. (2017). Measurements of seismic anisotropy in synthetic rocks with controlled crack geometry and different crack densities. *Pure & Applied Geophysics*, 174(5), 1–16.
- Gassmann, F. (1951). Über die Elastizität poröser Medien. *Vierteljahrsschr der Naturforschenden Gessellschaft in Zürich*, 96, 1–23.
- Grecheka, V., & Kachanov, M. (2006). Effective elasticity of rocks with closely spaced and intersecting cracks. *Geophysics*, 71(3), D85–D91.
- Guéguen, Y., & Kachanov, M., (2011). Effective elastic properties of cracked and porous rocks. In *Mechanics of crustal rocks*, CISM Courses and Lectures (Vol. 533). Berlin: Springer.
- Guéguen, Y., & Sarout, J. (2009). Crack-induced anisotropy in crustal rocks: predicted dry and fluid-saturated Thomsen's parameters. *Physics of the Earth and Planetary Interiors*, 172(1), 116–124.
- Guéguen, Y., & Sarout, J. (2011). Characteristics of anisotropy and dispersion in cracked medium. *Tectonophysics*, 503(1), 165–172.
- Hall, S. A., & Kendall, J. M. (2003). Fracture characterization at Valhall: Application of P-wave amplitude variation with offset and azimuth (AVOA) analysis to a 3D ocean-bottom data set. *Geophysics*, 68(4), 1150–1160.
- Hudson, J. A. (1981). Wave speeds and attenuation of elastic waves in material containing cracks. *Geophysical Journal of the Royal Astronomical Society*, 64, 133–150.
- Hudson, J. A., Liu, E., & Crampin, S. (1996). The mechanical properties of materials with interconnected cracks and pores. *Geophysical Journal International*, 124(1), 105–112.
- Hudson, J. A., Pointer, T., & Liu, E. (2001). Effective-medium theories for fluid-saturated materials with aligned cracks. *Geophysical Prospecting*, 49(5), 509–522.
- Jakobsen, M., & Chapman, M. (2009). Unified theory of global flow and squirt flow in cracked porous media. *Geophysics*, 74(2), WA65–WA76.
- Jakobsen, M., Hudson, J. A., & Johansen, T. A. (2003). T-matrix approach to shale acoustics. *Geophysical Journal International*, 154(2), 533–558.
- Liu, E., Chapman, M., Zhang, Z., & Queen, J. H. (2006). Frequency-dependent anisotropy: Effects of multiple fracture sets on shear-wave polarizations. *Wave Motion*, 44(1), 44–57.
- Liu, E., Hudson, J. A., & Pointer, T. (2000). Equivalent medium representation of fractured rock. *Journal of Geophysical Research: Solid Earth*, 105(B2), 2981–3000.
- Maultzsch, S., Chapman, M., Liu, E., & Li, X. Y. (2007). Modelling and analysis of attenuation anisotropy in multi-azimuth VSP data from the Clair field. *Geophysical Prospecting*, 55(5), 627–642.
- Mavko, G., Mukerji, T., & Dvorkin, J. (1998). *The Rock physics handbook: Tools for seismic analysis of porous media*. Cambridge: Cambridge University Press.
- Müller, T. M., Gurevich, B., & Lebedev, M. (2010). Seismic wave attenuation and dispersion resulting from wave-induced flow in porous rocks—A review. *Geophysics*, 75(5), 75A147–75A164.
- Norris, A. N. (1993). Low-frequency dispersion and attenuation in partially saturated rocks. *The Journal of the Acoustical Society of America*, 94(1), 359–370.
- Pride, S. R., & Berryman, J. G. (2003). Linear dynamics of double-porosity dual-permeability materials. I. Governing equations and acoustic attenuation. *Physical Review E*, 68(3), 036603.
- Rathore, J. S., Fjaer, E., Holt, R. M., & Renlie, L. (1995). P-and S-wave anisotropy of a synthetic sandstone with controlled crack geometry. *Geophysical Prospecting*, 43(6), 711–728.
- Sarout, J. (2012). Impact of pore space topology on permeability, cut-off frequencies and validity of wave propagation theories. *Geophysical Journal International*, 189(1), 481–492.
- Sarout, J., Cazes, E., Delle Piane, C., Arena, A., & Esteban, L. (2017). Stress-dependent permeability and wave dispersion in tight cracked rocks: Experimental validation of simple effective medium models. *Journal of Geophysical Research: Solid Earth*, 122, 6180–6201.
- Sayers, C. M., & Kachanov, M. (1995). Microcrack-induced elastic wave anisotropy of brittle rocks. *Journal of Geophysical Research: Solid Earth*, 100(B3), 4149–4156.
- Schoenberg, M. (1980). Elastic wave behavior across linear slip interfaces. *The Journal of the Acoustical Society of America*, 68(5), 1516–1521.
- Schoenberg, M., & Sayers, C. M. (1995). Seismic anisotropy of fractured rock. *Geophysics*, 60(1), 204–211.
- Smyshlyaev, V. P., Willis, J. R., & Sabina, F. J. (1993). Self-consistent analysis of waves in a matrix-inclusion composite—III. A matrix containing cracks. *Journal of the Mechanics and Physics of Solids*, 41(12), 1809–1824.
- Thomsen, L. (1995). Elastic anisotropy due to aligned cracks in porous rock. *Geophysical Prospecting*, 43(6), 805–829.
- Tillotson, P., Chapman, M., Sothcott, J., Best, A. I., & Li, X. Y. (2014). Pore fluid viscosity effects on P-and S-wave anisotropy in synthetic silica-cemented sandstone with aligned fractures. *Geophysical Prospecting*, 62(6), 1238–1252.
- Tillotson, P., Sothcott, J., Best, A. I., Chapman, M., & Li, X. Y. (2012). Experimental verification of the fracture density and shear-wave splitting relationship using synthetic silica cemented sandstones with a controlled fracture geometry. *Geophysical Prospecting*, 60(3), 516–525.
- Verdon, J. P., Angus, D. A., Michael, K. J., & Hall, S. A. (2008). The effect of microstructure and nonlinear stress on anisotropic seismic velocities. *Geophysics*, 73(4), D41–D51.
- Verdon, J. P., & Kendall, J. (2011). Detection of multiple fracture sets using observations of shear-wave splitting in microseismic data. *Geophysical Prospecting*, 59(4), 593–608.
- Wang, D., Qu, S. L., Ding, P. B., & Zhao, Q. (2017). Analysis of dynamic fracture compliance based on poroelastic theory. Part I: model formulation and analytical expressions. *Pure and Applied Geophysics*, 174(5), 2103–2120.
- Wang, D., Wang, L., & Ding, P. (2016). The effects of fracture permeability on acoustic wave propagation in the porous media: A microscopic perspective. *Ultrasonics*, 70, 266–274.
- Wang, D., & Zhang, M. G. (2014). Elastic wave propagation characteristics under anisotropic squirt-flow condition. *Acta*

- Physica Sinica*, 63(6), 69101. **(in Chinese with English abstract).**
- Wang, H. F. (2000). Theory of linear poroelasticity with application to geomechanics and hydrogeology. USA: Princeton University Press.
- White, J. E. (1983). *Underground sound: Application of seismic waves* (Vol. 253). Amsterdam: Elsevier.
- White, J. E., Mihailova, N., & Lyakhovitsky, F. (1975). Low-frequency seismic waves in fluid-saturated layered rocks. *The Journal of the Acoustical Society of America*, 57(S1), S30–S30.
- Winterstein, D. F. (1990). Velocity anisotropy terminology for geophysicists. *Geophysics*, 55(8), 1070–1088.
- Zatsepin, S. V., & Crampin, S. (1997). Modelling the compliance of crustal rock—I. Response of shear-wave splitting to differential stress. *Geophysical Journal International*, 129(3), 477–494.

(Received September 7, 2017, revised February 21, 2018, accepted February 23, 2018, Published online March 19, 2018)